

Energy Advances

Accepted Manuscript

This article can be cited before page numbers have been issued, to do this please use: B. R. Yenduri, V. K. Katta and C. A. Ohlin, *Energy Adv.*, 2026, DOI: 10.1039/D5YA00374A.



This is an Accepted Manuscript, which has been through the Royal Society of Chemistry peer review process and has been accepted for publication.

Accepted Manuscripts are published online shortly after acceptance, before technical editing, formatting and proof reading. Using this free service, authors can make their results available to the community, in citable form, before we publish the edited article. We will replace this Accepted Manuscript with the edited and formatted Advance Article as soon as it is available.

You can find more information about Accepted Manuscripts in the [Information for Authors](#).

Please note that technical editing may introduce minor changes to the text and/or graphics, which may alter content. The journal's standard [Terms & Conditions](#) and the [Ethical guidelines](#) still apply. In no event shall the Royal Society of Chemistry be held responsible for any errors or omissions in this Accepted Manuscript or any consequences arising from the use of any information it contains.

Carbon-coated niobium tungsten oxides as new and efficient anode materials for Na-ion batteries

Y. Bhaskara Rao*, Katta Vamsi Krishna, C. André Ohlin*

Department of Chemistry, Umeå University, Umeå 90187, Sweden

Open Access Article. Published on 15 April 2026. Downloaded on 4/15/2026 8:39:07 PM.
This article is licensed under a Creative Commons Attribution 3.0 Unported Licence.



Energy Advances Accepted Manuscript

*Corresponding authors: bhaskararaoyenduri@gmail.com , andre.ohlin@umu.se

Highlights

- Carbon-coated, TTB-type, niobium tungsten oxides, $\text{Nb}_{18}\text{W}_{16}\text{O}_{93}$ (Nb-rich) and $\text{Nb}_7\text{W}_{10}\text{O}_{47}$ (W-rich) are prepared by a facile hydrothermal-annealing method.
- Nb-rich material, NWO, delivered a high reversible capacity of $163.95 \text{ mA}\cdot\text{h}\cdot\text{g}^{-1}$ at a current density of $10 \text{ mA}\cdot\text{g}^{-1}$.
- Interestingly, W-rich material, WNO attained an impressive cycling stability with a high capacity retention of 81% at a current density of $100 \text{ mA}\cdot\text{g}^{-1}$ over 420 cycles.
- The slow capacity fading observed in the material, NWO is possibly caused by a significant increase in the charge transfer resistance during cycling.



Abstract

Tetragonal Tungsten Bronze (TTB)- type niobium–tungsten oxides are very interesting anode candidates for Na-ion battery applications due to their compositional flexibility, structural stability and large open-tunnel networks, which enable fast ion transport and pseudo capacitive behaviour. The present work introduces two TTB-type niobium tungstate anode materials, namely $\text{Nb}_{18}\text{W}_{16}\text{O}_{93}$ (Nb dominant) and $\text{Nb}_7\text{W}_{10}\text{O}_{47}$ (W dominant), prepared by a one-step hydrothermal method followed by a low-temperature calcination at 800 °C. Further, the low inherent electronic conductivity of the anode materials is effectively enhanced by incorporating the active materials with a carbon matrix to improve Na^+ -ion transport and storage. The presence of uniform carbon-coating surrounding the active particles in both materials is confirmed by high-resolution transmission electron microscopy images. At a current density of 10 $\text{mA}\cdot\text{g}^{-1}$ the carbon-coated $\text{Nb}_{18}\text{W}_{16}\text{O}_{93}$ (NWO) delivered a higher reversible capacity of 163.95 $\text{mA}\cdot\text{h}\cdot\text{g}^{-1}$ compared to that of the carbon-coated $\text{Nb}_7\text{W}_{10}\text{O}_{47}$ (WNO) (127.55 $\text{mA}\cdot\text{h}\cdot\text{g}^{-1}$). Interestingly, the WNO material showed a remarkable cycling stability over 420 cycles, at a current density of 100 $\text{mA}\cdot\text{g}^{-1}$, recording a higher capacity retention of 81%, compared to NWO (69%). The promising electrochemical performance of the materials is related to structural defects, specific surface areas, charge transfer resistances during charge/discharge cycles and Na^+ -ion diffusion coefficients. Thus, the current work introduces niobium tungsten oxides as new and efficient anode candidates for sodium ion battery technology, and also enables safe, economical, and long-cycling Na-ion batteries, ultimately supporting the transition toward more sustainable energy technologies.

Keywords: *Anode material; Sodium-ion battery; Carbon coating; Niobium tungsten oxides; Tetragonal tungsten bronze; $\text{Nb}_{18}\text{W}_{16}\text{O}_{93}$; $\text{Nb}_7\text{W}_{10}\text{O}_{47}$*



1. Introduction

Sodium-ion batteries (SIBs) have several intrinsic advantages over lithium ion batteries (LIBs), making them promising in large-scale energy storage systems (ESS) as sodium is cheaper and more readily available than lithium.^{1,2} The majority of SIB research has been devoted to investigating stable and inexpensive cathode materials, such as Prussian blue, NaFePO₄, and NaNi_{0.5}Mn_{0.5}O₂.^{3,4} Most of the ongoing efforts to explore anode materials are limited to non-graphitic carbonaceous materials. Because of its disordered structure and high interlayer distance, hard carbon is currently the best non-graphitic carbonaceous material for Na⁺-ion storage.⁵ Nonetheless, non-graphitic carbonaceous materials have certain drawbacks, including a high irreversible capacity and low capacity retention.

Metal oxides have been investigated and developed widely as alternatives to carbon-based anodes in SIBs due to their high theoretical capacity.⁶ Among them, oxides based on niobium are of great interest, due to their better physico-chemical characteristics and potential usage in energy-storage devices. In addition, they have a high working potential (>1.0 V) that can inhibit the formation of sodium dendrites and ensure the safety of operational batteries.⁷ Nevertheless, the low intrinsic electrical conductivity of many niobium-based oxides (*ca* 3.4×10^{-6} S cm⁻¹ at 300 K) decreases the alkali ion diffusion rate and restricts their application as substitutes for commercial anode materials.⁸ Carbon coating of the active material is found to be an economically feasible, simple, and practical method among the different approaches investigated to improve the electronic conductivity.⁹

Several articles were reported on the incorporation of carbon matrix around active particles to improve the electronic conductivity, thereby enhancing the electrochemical performance of the materials. For instance, our group recently reported a solution-assisted solid-state process to



prepare fluorine-doped and carbon-coated KNb_3O_8 material, which delivered a discharge capacity of $173 \text{ mA}\cdot\text{h}\cdot\text{g}^{-1}$ at a current density of $10 \text{ mA}\cdot\text{g}^{-1}$.¹⁰ In this case, polyvinylidene fluoride (PVDF), a commonly used binder in SIBs/LIBs, is used for both carbon and fluorine source. Chen *et al.* reported a composite of $\text{TT-Nb}_2\text{O}_5$ and CNT (glucose-derived carbon) synthesized by a one-step hydrothermal method followed by annealing. The material delivered a high specific capacity of $203 \text{ mA}\cdot\text{h}\cdot\text{g}^{-1}$ at $0.2 \text{ A}\cdot\text{g}^{-1}$ and a capacity retention of $\sim 135 \text{ mA}\cdot\text{h}\cdot\text{g}^{-1}$ at $0.2 \text{ A}\cdot\text{g}^{-1}$ after 300 cycles.¹¹ Using polyacrylonitrile as a carbon and nitrogen source, a sonochemical method was employed to prepare core-shell structured $\text{Nb}_2\text{O}_5@\text{NC}$ nanoparticles.¹² After 200 cycles at 0.2 C the nanocomposite exhibited a discharge capacity of $96 \text{ mA}\cdot\text{h}\cdot\text{g}^{-1}$, which is a notable improvement over the undoped sample ($28 \text{ mA}\cdot\text{h}\cdot\text{g}^{-1}$).

Here we report niobium tungsten oxide materials as new anode candidates in SIBs for the first time. The benefits of niobium tungsten oxide anodes include long-term capacity retention, and high energy and power densities. Additionally, they offer enhanced electrochemical performance as well as improved safety at low temperatures.¹³ These advantages result from stable crystal structures and excellent mobile-ion diffusion coefficients. Generally, niobium oxides are known for their robust frameworks and pseudo capacitive sodium-storage behavior but suffer from limited electronic conductivity, whereas tungsten oxides exhibit relatively higher electronic conductivity yet inferior structural stability during cycling. The combination of Nb and W within a single oxide framework effectively integrates the advantages of both components, leading to improved charge transport and electrochemical kinetics. Further, incorporating tungsten into the niobium oxide framework offers a promising strategy to enhance the electronic transport and stabilize open crystallographic shear structures.¹⁴ However, systematic studies correlating the crystallographic shear architecture of niobium-tungsten oxides with Na-storage kinetics remain scarce. This work



addresses this gap by investigating representative Nb-W-O shear phases and elucidating their structure-property-performance relationships in Na⁺-ion batteries. In this work, two niobium tungsten oxide materials: Nb₁₈W₁₆O₉₃ (Nb rich) and Nb₇W₁₀O₄₇ (W rich) were chosen to investigate the influence of Nb and/or W on the overall performance of the SIB half cells. Both belong to pseudo-tetragonal tungsten bronze orthorhombic superstructures which generally consists of corner-sharing octahedra (MO₆), which are arranged in such a way that trigonal, square, and pentagonal tunnels arise.¹⁵ The Nb-rich phase contains partially occupied pentagonal tunnels with metal-oxygen strings, whereas the W-dominant phase contains more open or less occupied tunnels resulting from its higher oxygen content compared to the Nb-richer phases.¹⁶ The availability of sites for ion storage and improved diffusion speed are directly affected by the degree to which these tunnels are occupied, with the main difference between the two structures lying in their oxygen-to-metal ratio which ultimately decides the occupation of mobile-ion diffusion channels within their shared tetragonal tungsten bronze (TTB)-type framework.

The two materials, Nb₁₈W₁₆O₉₃ and Nb₇W₁₀O₄₇ are prepared by a simple hydrothermal method followed by low-temperature calcination. Although 800 °C is high in absolute terms, for this niobium tungsten oxide system, this method represents a relatively mild lower-temperature route compared to traditional solid-state methods (>1000 °C), which is beneficial for energy savings and suppressing excessive grain growth. It was previously reported that the cation-ordering in low-temperature niobium-rich NbWO bronzes, where the new structures were synthesized at 800-900 °C, indicating that this temperature enables formation of complex Nb-W oxides without resorting to much higher (>1000 °C) processing.¹⁷ Further, both materials are coated with carbon, using sucrose as a carbon source, as it easily soluble in water without affecting the pH, inexpensive, and yields uniform carbon coatings on inorganic particles upon pyrolysis,¹⁸ which further improve



the electrochemical performance of the electrodes. The structure, morphology, specific surface area, disordered/defective nature, Na⁺-ion diffusion coefficient, and the contribution of capacitive and diffusive behaviour are all examined in this work and compared in relation to the transport and storage behaviour of Na⁺ ions in the materials. X-ray diffraction (XRD), scanning electron microscopy (SEM), and transmission electron microscopy (TEM) were used to investigate the crystalline structure and morphology of the samples, respectively. Raman spectroscopy was used to study the vibrational modes as well as the D and G bands. Further, N₂ adsorption/desorption isotherms were utilized to analyze the specific surface area and pore size distributions. Cyclic voltammetry (CV), galvanostatic charge/discharge cycles, Nyquist impedance plots and the total capacitance partition curves were employed to study the electrochemical performance of the materials.

2. Experimental section

2.1 Material synthesis

Carbon-coated Nb₁₈W₁₆O₉₃ and Nb₇W₁₀O₄₇ (nominal composition: Nb₇W₁₀O_{47.5}) materials were prepared by a simple hydrothermal method followed by calcination. In a typical reaction, stoichiometric ratios of niobic acid (Nb₂O₅·*n*H₂O, >99%, 40% H₂O w/w; received as a gift from Prof. William H. Casey at UC Davis) and tungsten oxide (WO₃, 99.9%, TCI) were mixed with sucrose (C₁₂H₂₂O₁₁, >99%, TCI, 1 g) in 50 ml de-ionized water in a Teflon liner. It was then magnetically stirred for 1 h prior to heating at 180 °C for 12 h. After cooling to room temperature, the product was filtered and dried at 100 °C in a drying oven. Finally, the material was calcined at 800 °C for 4 h under N₂ atmosphere to obtain the final carbon-coated Nb₁₈W₁₆O₉₃ and Nb₇W₁₀O₄₇ samples. These carbon-coated samples were then referred to as **NWO** (Nb-rich) and **WNO** (W-rich), respectively.



2.2 Material characterization

XRD using Cu- K_{α} radiation on a Bruker D8 Advance diffractometer with the detector model: LYNXEYE XE-T operated at 40 kV/40mA in 1D mode was used to analyze the crystal structure of the materials. The samples were scanned at a step size of 0.01945° in the 2θ range of $10-80^{\circ}$. The Raman spectra were recorded using a Renishaw Qontor device (Renishaw Plc, UK) running WiRe (version 5.6). Using a 5x lens in normal confocality mode, a 405 nm solid state laser with a nominal maximum power of 40 mW was employed. The spectral range was centered at 1400 cm^{-1} , and 10s exposure times were used. SEM images were obtained on a Zeiss Evo SEM instrument equipped with an HDBSD detector. The energy-dispersive X-ray spectroscopy (EDX) images were taken with the help of X-MaxN 80 mm² silicon drift detector. FEI Glacios 200 kV cryo-TEM with a Ceta-D 4k x 4k CMOS detector was used to get the TEM images, and the TEM grids were obtained on a Quantifoil R2/1 micro machined holey carbon grids (300 mesh copper). For selected area electron diffraction (SAED) pictures, an aperture of 10 μm was used. A Micromeritics TriStar 3000 porosimeter was used to measure the N₂ adsorption-desorption and the isotherms were recorded at -196°C after the samples were outgassed for two hours at 100°C . The specific surface areas were collected using the Brunauer-Emmett-Teller (BET) method, and the pore volumes were computed using the desorption isotherms. The pore size distributions were estimated using the Barret, Joyner, and Halenda (BJH) algorithm and the ASAP-2010 program.

2.3 Electrochemical characterization

CR-2032 coin-type half-cells were prepared for the electrochemical experiments in an Ar-filled glove box (Mbraun, MB10 compact) with O₂ and H₂O levels < 0.5 ppm. The active material (80 wt%), Super P (Thermo Scientific) (10 wt%), and sodium carboxymethylcellulose (CMC-MedChemExpress; 10 wt%) binder were mixed with de-ionized water to prepare a slurry. After



applying the mixture on a copper foil current collector (TMAXCN; 14 mm in diameter and 0.1 mm in thickness), it was dried at 50 °C. The electrode had an average mass loading of 2 - 3 mg·cm⁻². The liquid electrolyte was 1 M NaClO₄ (Thermo Scientific) in ethylene carbonate (EC, from AmBeed) and dimethyl carbonate (DMC, from TCI; 1:1 v/v), and the separator was a glass microfibre filter (Whatman, Grade GF/D; 19 mm diameter). The counter/reference electrode was Na metal. A Solartron Modulab 2100A workstation was used to record the CV curves (0.01–2.5 V) at different scan rates and electrochemical impedance spectroscopy (EIS) in the frequency range of 100 mHz to 100 kHz. The galvanostatic charge-discharge curves were recorded using a NEWARE CT-4008 battery tester within a voltage window of 0.01–2.5 V (vs Na⁺/Na). Every electrochemical measurement was performed at 20 °C.

3. Results and Discussion

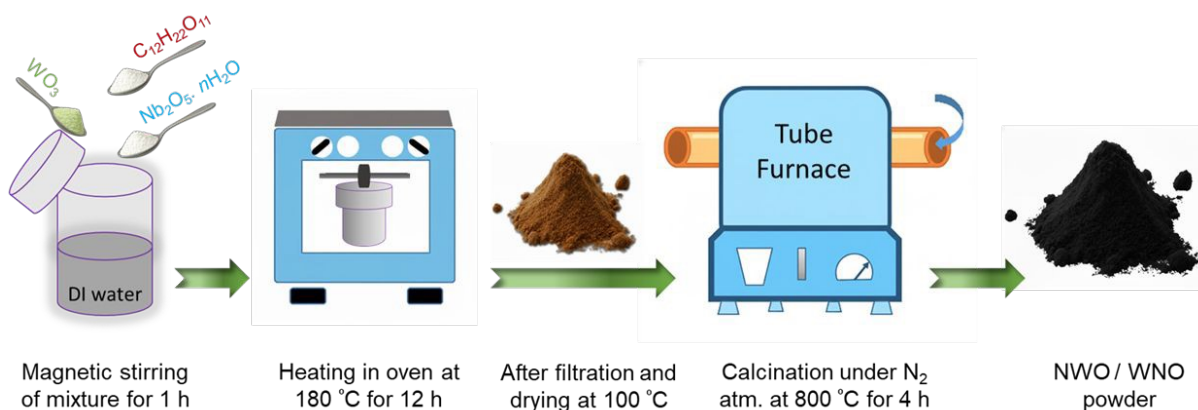


Figure 1. Schematic diagram for the preparation of NWO/WNO samples.

The schematic of the synthesis of niobium tungsten oxides via a simple hydrothermal method followed by low-temperature calcination (800 °C) is shown in **Fig. 1**.



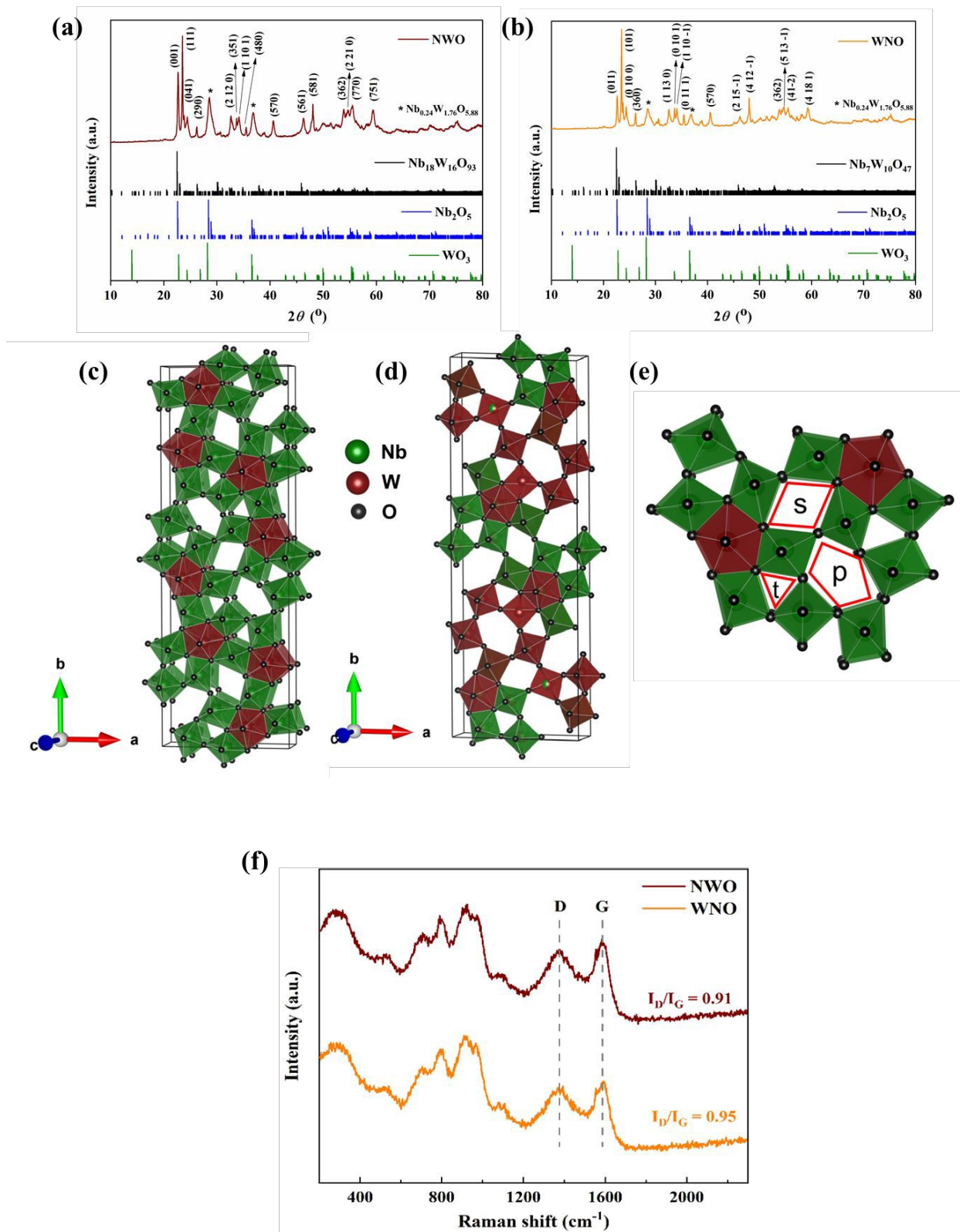


Figure 2. XRD patterns (**a** and **b**), crystal structure (**c** and **d**) of NWO and WNO materials, **e**) representation of trigonal (t), square (s), and pentagonal (p) tunnels in NWO and **f**) Raman spectra of NWO and WNO materials.

Fig. 2a and **b** display the XRD patterns of the materials, NWO and WNO, and the sharp diffraction peaks indicate that both materials have good crystallinity. Major reflections of NWO sample are associated with the distorted TTB crystal structure with *Pbam* space group ($\text{Nb}_{18}\text{W}_{16}\text{O}_{93}$ - COD# 2107344).¹⁹ While, the reflections of the sample WNO are related to an orthorhombic crystal structure with *P2₁2₁2* space group ($\text{Nb}_7\text{W}_{10}\text{O}_{47}$ - COD# 1521454),²⁰ and a minor intermediate tetragonal phase, $\text{Nb}_{0.24}\text{W}_{1.76}\text{O}_{5.88}$ (COD# 1522265) is also observed in both of the materials. Further, the reference patterns of Nb_2O_5 (COD# 2106534) and WO_3 (COD# 1004057) are presented in **Fig. 2a** and **b** for comparison. The orthorhombic NWO is a $1 \times 3 \times 1$ superstructure of the typical tetragonal tungsten bronze (**Fig. 2c**). In addition to the distorted octahedra of the tetragonal tungsten bronzes, the superstructure is produced by partially filling pentagonal tunnels with $-\text{M}-\text{O}-$ chains to form pentagonal bipyramids.¹³ On the other side, an important feature of WNO structure (**Fig. 2d**) is that the pentagonal tunnels are nearly regular pentagons when they are occupied by M-O chains, whereas the unoccupied pentagonal tunnels are much more deformed.²⁰ The trigonal (t), square (s), and pentagonal (p) tunnels emerging from the arrangement of corner-sharing octahedra (MO_6) are represented in **Fig. 2e**. Further, **Fig. 2f** shows the Raman spectra used to examine the degree of disorder and vibrational energy modes in both samples. The band observed at *ca* 290 cm^{-1} is attributed to O-W-O deformation and the one around 800 cm^{-1} corresponds to the stretching mode of O-W-O.²¹ The bands occurred in between 380 and 800 cm^{-1} are associated with the stretching modes inside the NbO_6 octahedra.²² The two more peaks at *ca*



900 and 975 cm^{-1} may correspond to the WO_6 and NbO_6 octahedra, respectively.²³ Additionally, Raman spectroscopy allows for the use of the D band to G band intensity ratio (I_D/I_G) as a metric to evaluate the degree of disorder and defects in carbon-based materials. The structural defects can increase the ion and electron accessibility through the enhanced surface area and porosity of carbon materials.²⁴ In this case, the graphitic structure is characterized by the G band at *ca* 1580 cm^{-1} , whereas the disorder-induced vibrations give rise to the D band at about 1380 cm^{-1} , showing the existence of defects. From **Table 2**, it is apparent that the I_D/I_G ratio of both materials is found to be close to 1, suggesting a significant number of defects, such as vacancies, edges, and other structural imperfections in the materials. Thus, the amorphous nature present in the carbon-coated samples, introduced by the structural defects, can significantly enhance the electronic conductivity of the niobium tungsten oxide materials.



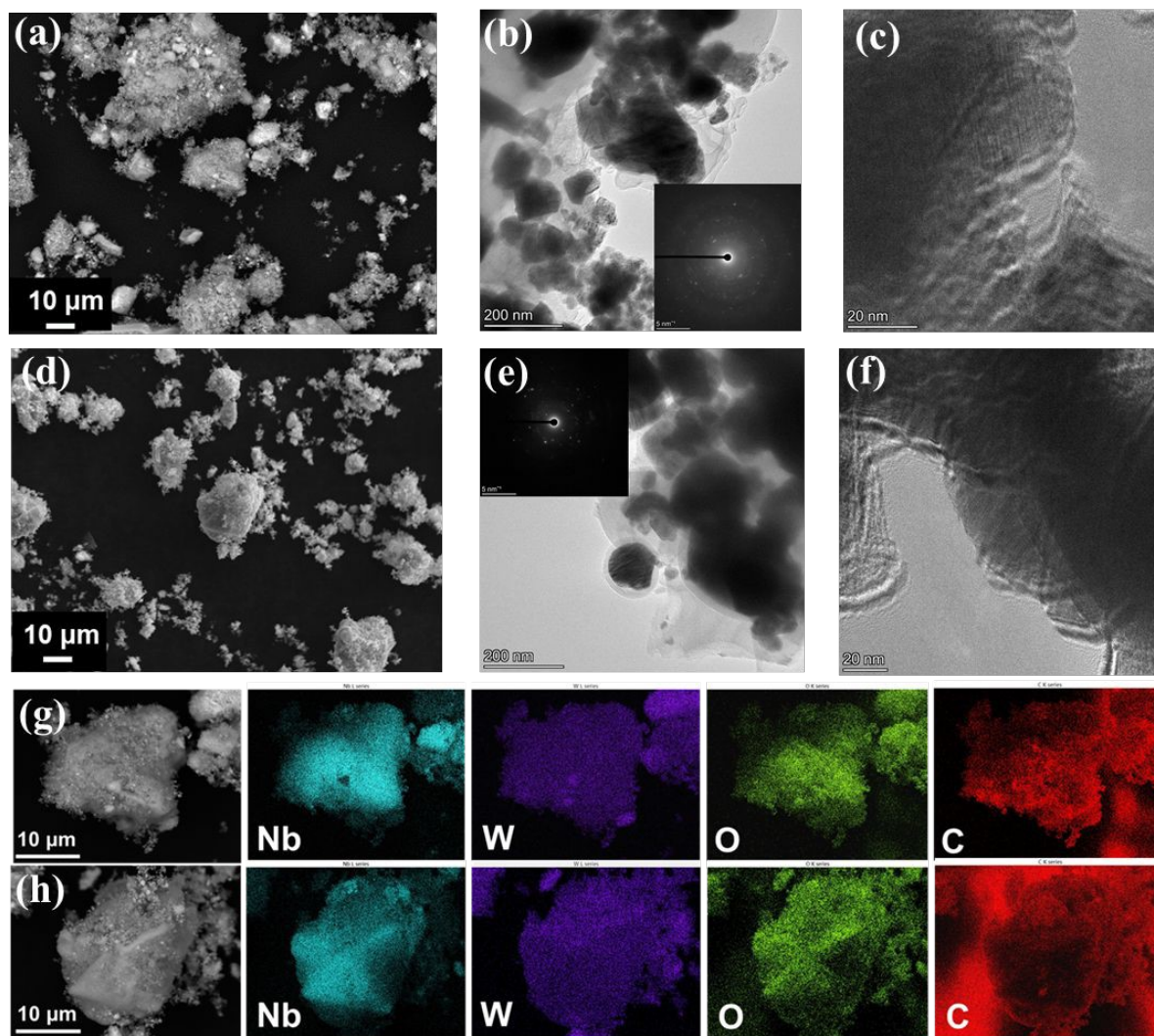


Figure 3. SEM (a, d), TEM (b, e) and high-resolution transmission electron microscopy (HRTEM) (c, f) images of (a-c) NWO, and (d-f) WNO samples (inset: SAED pattern), and EDX images of (g) NWO and (h) WNO materials.

SEM and TEM were used to examine the morphology and microstructure of the NWO and WNO materials (Fig. 3). It is evident from Fig. 3a and d that both samples contain irregularly shaped and micron-sized particles. The particles exhibit porous surfaces, which may enhance the



electrolyte penetration and ion diffusion. The selected area electron diffraction (SAED) pattern shows the crystal orientations of NWO (inset: **Fig. 3b**) and WNO (inset: **Fig. 3e**) materials. In particular, the bright spots and the hollow ring pattern observed in the SAED images suggest that the active particles are surrounded by an amorphous or disordered carbon framework.^{25,26} The carbon-coating, thus, prevents the particle agglomeration and improves the electronic pathways. The HRTEM images (**Fig. 3c** and **f**) further reveal the well-resolved lattice fringes in both materials, demonstrating their crystalline nature. Thus, the thin amorphous layer that surrounds the active particles in the HRTEM images indicates that the niobium tungsten oxides have been successfully integrated and adorned with the carbon matrix. Finally, the homogeneous distribution of the elements, Nb, W, O, and C in both carbon-coated materials is confirmed by the EDX elemental mapping images, which are seen in **Fig. 3g** and **h**. Here, phase separation and/or element-rich clusters are not observed, confirming the effective integration of elements.



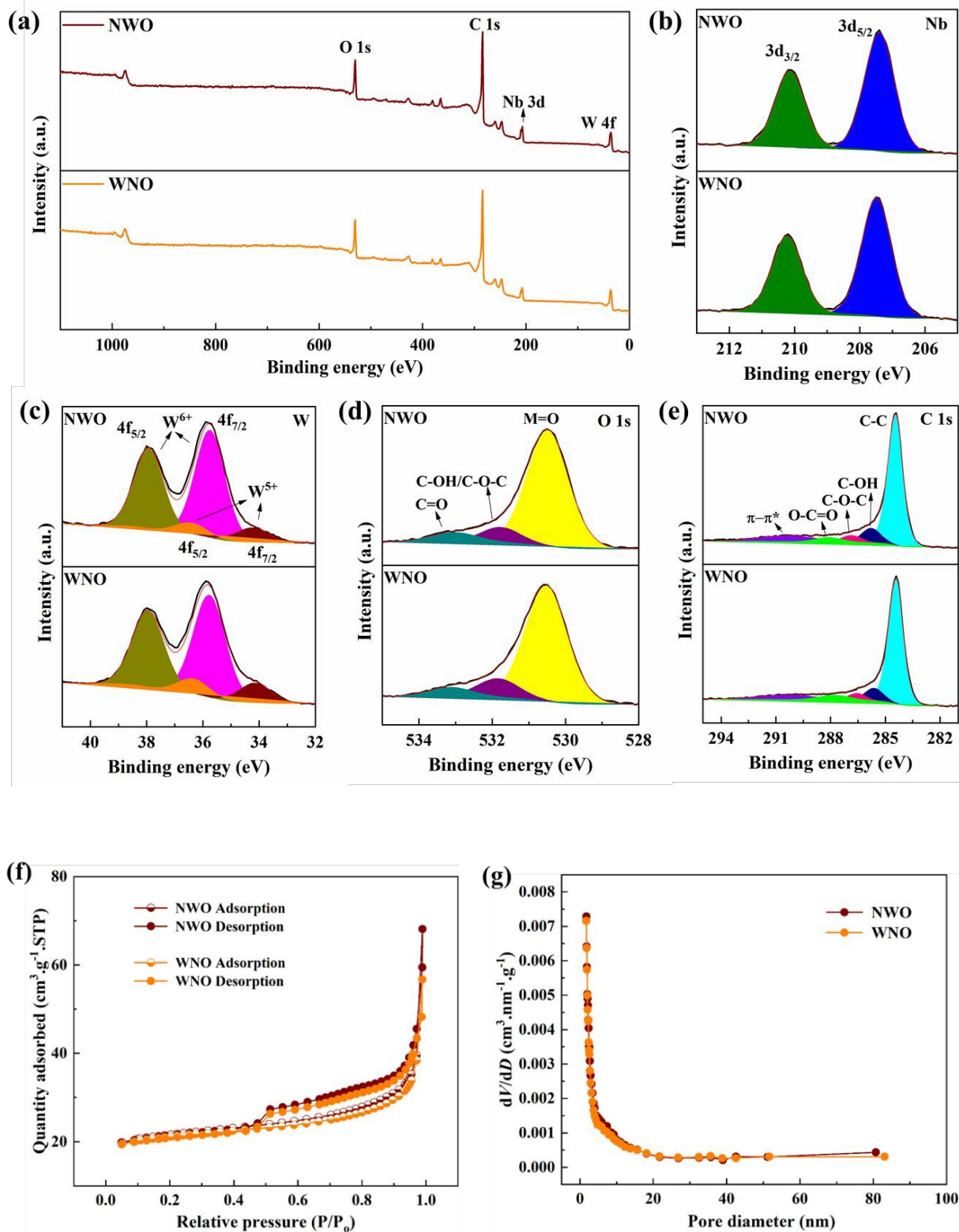


Figure 4. **a)** XPS survey spectra, **b)** Nb 3d, **c)** W 4f, **d)** O 1s and **e)** C 1s spectra, **f)** N₂-adsorption and desorption isotherms, and **g)** pore size distribution of NWO and WNO materials.

XPS analysis was used to identify the valence states and surface characteristics of NWO and WNO samples and the presence of elements, Nb, W, O and C in both samples is confirmed by XPS survey spectra (**Fig. 4a**). Further, two main peaks, appeared in **Fig. 4b** at 207.5 and 210.2 eV, correspond to Nb 3d_{5/2} and 3d_{3/2}, respectively.²⁷ The XPS spectra of W (**Fig. 4c**) exhibit characteristic peaks at 35.7 and 38.0 eV, which are assigned to the W⁶⁺ 4f_{7/2} and 4f_{5/2}, spin-orbit components, respectively. In addition, the peaks located at 34.1 and 36.4 eV correspond to the W⁵⁺ 4f_{7/2} and 4f_{5/2} states. Here, the presence of W⁵⁺ indicates partial reduction of tungsten, which may enhance the electronic conductivity by generating oxygen vacancies and defect sites that facilitate charge transport.²⁸ In both samples, the O 1s peak (**Fig. 4d**) deconvolutes into three peaks, metal-oxide (M=O), C-OH/C-O-C, and C=O which are centered at the binding energies of 530.5, 531.9 and 533.1 eV, respectively. Finally, a high-resolution C 1s XPS spectra (**Fig. 4e**) consist of C-C, C-OH, C-O-C, O-C=O, and $\pi-\pi^*$ peaks at 284.4, 285.8, 286.9, 288.2, and 290.5 eV, respectively.²⁷ The surface area and porosity of the synthesized NWO and WNO samples were measured using N₂ adsorption–desorption isotherms (**Fig. 4f** and **g**). The NWO sample had a specific surface area of 68.35 m² g⁻¹, while the WNO sample had a specific surface area of 66.64 m² g⁻¹, and both of the samples possess similar micropore volumes of 0.0242 cm³ g⁻¹. It was reported previously that the carbon coating can effectively reduce the agglomeration of bulk materials and enhance the surface area of the samples.²⁹ As a result, it increases the number of active sites for ion adsorption, as well as enabling easy and free transportation of electrolyte ions through the formation of aligned pore



channels.³⁰ Further, the Barrett–Joyner–Halenda (BJH) mean pore diameters (**Fig. 4g**) of NWO and WNO samples are found to be 6.2 and 5.3 nm, respectively. Thus, the structures with wide surface areas can mitigate the evolution of stress produced during the ion insertion/extraction process, buffer volume change, and shorten the transport distance for ion diffusion.³⁰

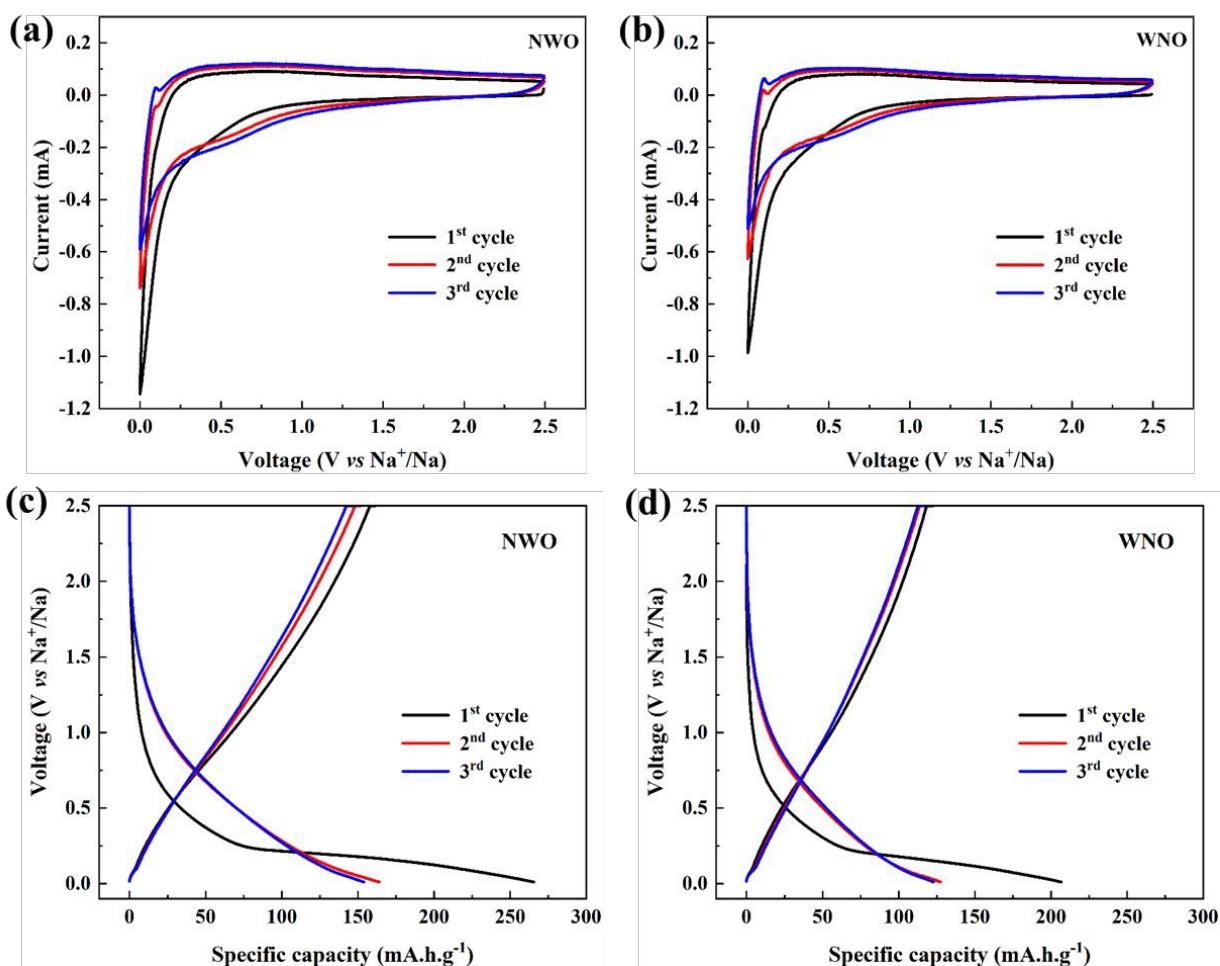


Figure 5. CV curves of **a)** NWO, and **b)** WNO materials for the initial three cycles at a scan rate of 0.2 mV s^{-1} , and galvanostatic charge/discharge curves for **c)** NWO, and **d)** WNO materials for the first three cycles at a current density of 10 mA g^{-1} .



The cyclic voltammogram curves for NWO and WNO electrodes for the three initial cycles, in the voltage range of 0.01 to 2.5 V, at a scan rate of 0.2 mV s⁻¹ are displayed in **Fig. 5a** and **b**. A pair of sharp redox peaks appearing near 0.1 V in both materials are attributed to the insertion and extraction process of Na. A broad reduction peak appearing near 0.6 V is due to the irreversible reaction of the electrolyte which leads to the formation of the solid-electrolyte interface (SEI) layer on the electrode surface in both samples.²⁷ However, a significant stability is maintained during the subsequent cycles, which is evident from the overlapping CV traces. Further, **Fig. 5c** and **d** demonstrate the electrochemical performance of both samples at a current density of 10 mA g⁻¹ for the initial three charge-discharge cycles. The NWO electrode exhibited high initial discharge/charge specific capacities of 265.5/161.3 mA·h·g⁻¹, respectively, while the WNO electrode delivered initial discharge/charge capacities of 206.7/122.5 mA·h·g⁻¹, respectively. Here, both materials exhibited a low initial coulombic efficiency (ICE) of *ca* 60%, and it could be due to their large specific surface areas (**Table 2**), which influences the development of SEI layer during the first cycle. As a result, a significant irreversible capacity loss occurs in the first cycle; however, both materials displayed greatly improved electrochemical performance during the subsequent cycles by recording high coulombic efficiencies of *ca* 95%.



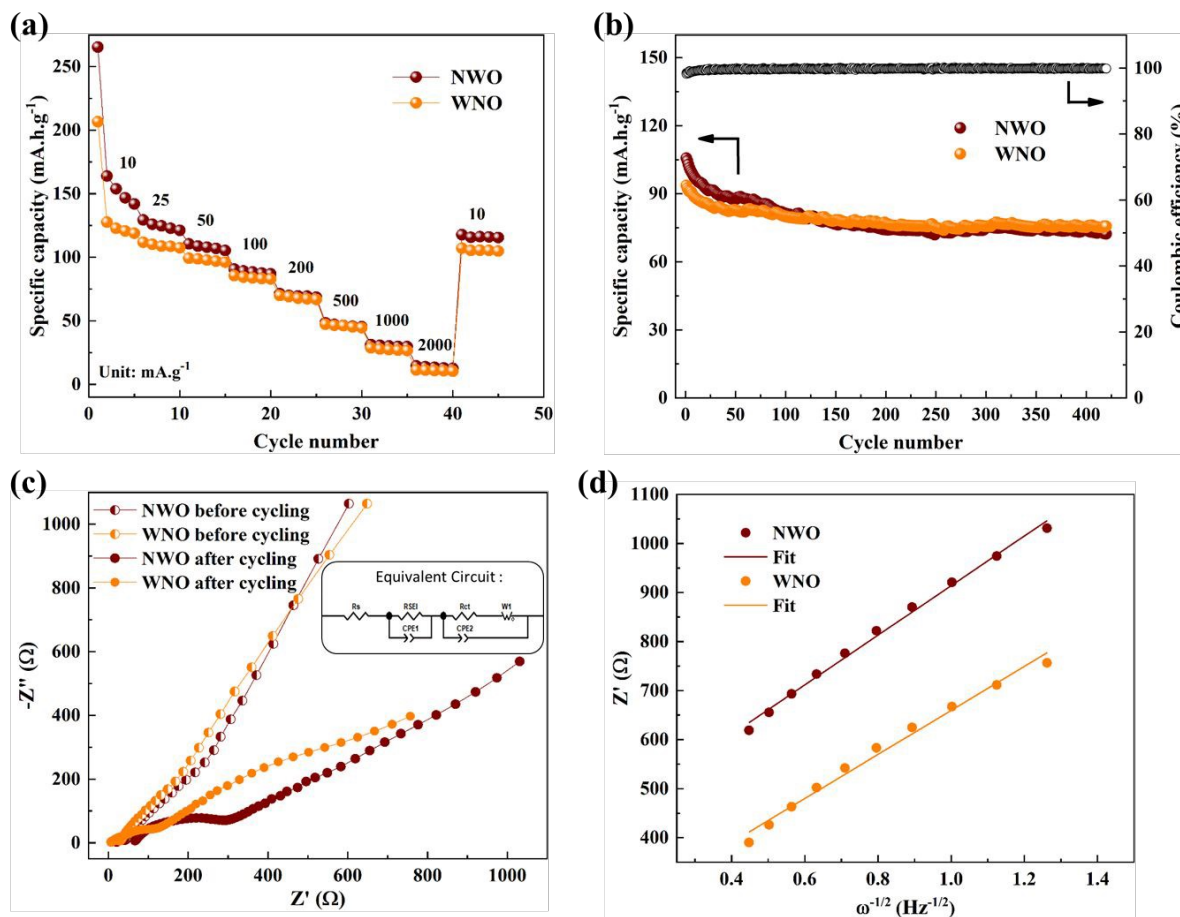


Figure 6. a) Rate capability at different current densities, b) long-term cycling performance at a current density of $100 \text{ mA}\cdot\text{g}^{-1}$, c) EIS, before and after cycling (inset: equivalent circuit), and d) fitting curves of Z' vs $\omega^{-1/2}$ at a low frequency region of NWO and WNO samples.

Fig. 6a displays the rate performance of NWO and WNO electrodes at different current densities. The NWO sample delivered high discharge specific capacities of 163, 129, 110, 90, 71, 48, 31 and $14 \text{ mA}\cdot\text{h}\cdot\text{g}^{-1}$ at current densities of 10, 25, 50, 100, 200, 500, 1000, and $2000 \text{ mA}\cdot\text{g}^{-1}$, respectively, whereas, WNO delivered the discharge specific capacities of 127, 111, 99, 85, 69, 47, 28 and $11 \text{ mA}\cdot\text{h}\cdot\text{g}^{-1}$, respectively, at the same current densities. Here, at low current densities, NWO delivered



slightly higher specific capacities compared to WNO, probably due to a small difference in their specific surface area (S_{BET}) and mean pore diameter (**Fig. 4a** and **b**). However, at higher current rates, both materials delivered nearly similar discharge capacities. It may instead arise from limits Na^+ -ion diffusion and electrochemical kinetics, which dominate in both cases, rather than from the specific material properties of the electrodes. Cycling at high current rates does not damage the structure of either of the carbon-coated electrodes, since a considerable amount of specific capacity is still retained even when the current density is restored to 10 mA g^{-1} , which indicates a superior rate performance for both samples. Thus, better reversibility and stability are attained in the WNO sample (84%), compared to NWO (72%).

Further, at a current density of 100 mA g^{-1} the electrochemical performance of both samples is observed for long-term cycling (**Fig. 6b**). After 420 cycles, the NWO electrode delivered a discharge specific capacity of 72 mA h g^{-1} , which only represents a 69% capacity retention. In contrast, WNO (76 mA h g^{-1}) demonstrated an impressive 81% capacity retention even after 420 cycles. Nonetheless, the coulombic efficiency of both materials is nearly 100%. This study employed a relatively low electrode loading to investigate the intrinsic properties of the materials. Future work will focus on optimizing electrode fabrication to achieve higher mass loadings and validate the practical application potential in full-cell configurations.

Now, the electrochemical performances of NWO and WNO samples are compared with that of some other reported niobium and/or tungsten based anode materials for SIBs in **Table 1**. As summarized in **Table 1**, the present materials demonstrate competitive electrochemical performance compared to previously reported niobium/tungsten-based oxide anodes. In particular, they exhibit improved cycling stability with minimal capacity fading over prolonged cycles, indicating excellent structural robustness during repeated sodiation/desodiation. Additionally, the



materials deliver favorable rate capability, retaining a significant fraction of the capacity even at higher current densities, which highlights their fast charge transport kinetics. These advantages can be attributed to the optimized composition and microstructure, which facilitate efficient ion diffusion and enhanced electronic conductivity.

Table 1. Comparison of electrochemical performances of NWO and WNO samples with the other reported Nb/W based anode materials for SIBs.

Material	Preparation	Potential window (V vs. Na ⁺ /Na)	Current density (mA·g ⁻¹)	Number of cycles	Capacity retention (%)	Reference
NbO ₂	Solid-state method	0.01 – 2.5	50	500	70	31
Nb ₂ O ₅ @WS ₂ @C	Electrospinning-Hydrothermal	0.01 – 3.0	1000	200	62	32
Nb-Ti octahedral molecular sieves (Cd-NTO)	Hydrothermal	0.01 – 2.5	50	100	72	33
W-Nb ₂ O ₅ /C	Hydrothermal	0.01 – 3.0	100	100	70	34
NWO	Hydrothermal	0.01 – 2.5	100	420	69	This work
WNO	Hydrothermal	0.01 – 2.5	100	420	81	This work

Analysis by electrochemical impedance spectroscopy (**Fig. 6c**) provides a clear understanding of the high and stable performance observed in the WNO sample. An equivalent circuit, used to match the Nyquist plots for both samples, before and after 20 cycles is shown in the inset of **Fig. 6c**, and it consists of a solution resistance (R_s), SEI layer resistance (R_{SEI}), and a charge transfer resistance



(R_{ct}). Both NWO and WNO electrodes exhibited similar charge transfer resistances of *ca* 30 Ω before cycling. However, a very higher charge transfer resistance of 329.7 Ω is recorded for the NWO sample compared to that of WNO (172.5 Ω), after 20 cycles. This may be the key to the slow capacity fading seen in case of NWO. Thus, the electrochemical performance of carbon-coated samples is influenced by SEI/charge transfer resistance during long-term cycling.

Additionally, equation 1 can be used to compute the Na^+ -ion diffusion coefficient, D_{Na^+} , which is directly related to the electrochemical stability and the charge transfer resistance.³⁵

$$D_{\text{Na}^+} = \frac{R^2 T^2}{2A^2 n^4 F^4 C_{\text{Na}^+}^2 \sigma^2} \quad (1)$$

where R is the gas constant, T is the temperature, A is the effective working area of the electrode, n is the number of transferred electrons, F is the Faraday constant, C represents the Na^+ -ion concentration, and σ is the slope of Z' vs $\omega^{-1/2}$, which is obtained by using equation 2,

$$Z' = R_s + R_{SEI} + R_{ct} + \sigma \omega^{-1/2} \quad (2)$$

Here, the slope (σ) can be calculated by using the plot between Z' and $\omega^{-1/2}$ (**Fig. 6d**). Z' is the real part of impedance, σ is the Warburg factor, and ω is the angular frequency.³⁶ The NWO electrode showed a Na^+ -ion diffusion coefficient of $6.4 \times 10^{-14} \text{ cm}^2 \cdot \text{s}^{-1}$, comparable with the reported value for Nb_2O_5 ,³⁷ after all the values were substituted, while the WNO electrode obtained significantly a higher Na^+ -ion diffusion coefficient of $8.2 \times 10^{-14} \text{ cm}^2 \cdot \text{s}^{-1}$. Thus, the transfer of Na^+ -ions is a little bit faster in case of WNO.

Table 2. Comparison of I_D/I_G ratio, specific surface area (S_{BET}), reversible discharge capacity at 10 mA g^{-1} , charge transfer resistance (R_{ct}) after 20 cycles and Na^+ -ion diffusion coefficient for NWO and WNO samples.



Material	I_D/I_G	S_{BET} ($m^2 g^{-1}$)	Discharge capacity at 10 mA g^{-1} (mA·h· g^{-1})	R_{ct} (Ω)	Diffusion coefficient ($cm^2 \cdot s^{-1}$)
NWO	0.91	68.35	163.95	329.7	6.4×10^{-14}
WNO	0.95	66.64	127.55	172.5	8.2×10^{-14}



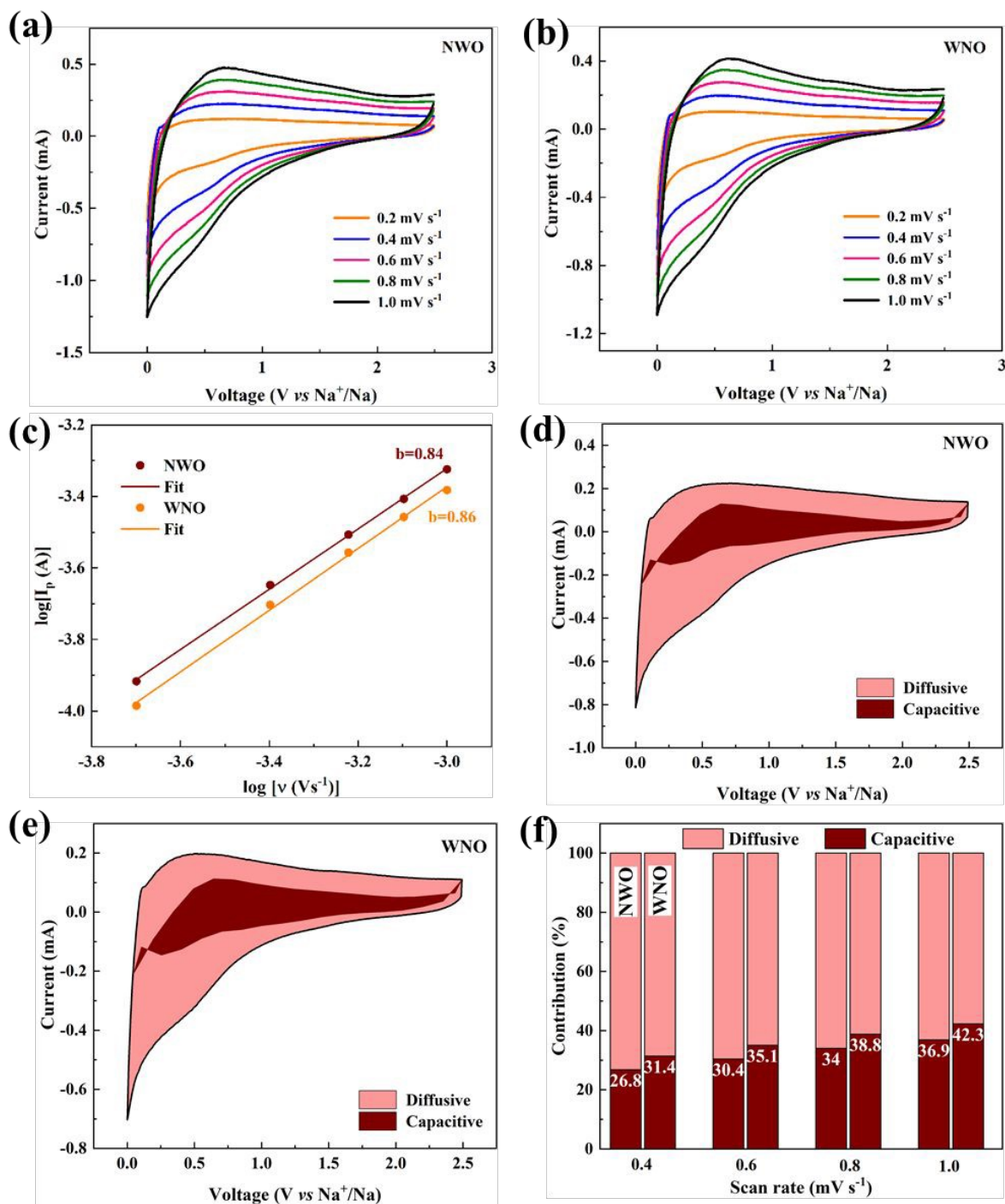


Figure 7. CV curves at different scan rates for **a)** NWO and **b)** WNO materials, **c)** the logarithmic relationship between the scan rates and peak currents in NWO and WNO materials, CV curve showing the diffusion-controlled and capacitive contribution in **d)** NWO, and **e)** WNO materials



at 0.4 mV·s⁻¹ scan rate, and **f**) contribution ratio of diffusion-controlled and capacitive process to the total capacity at different scan rates for NWO and WNO materials.

Fig. 7a and **b** display the CV plots of the NWO and WNO materials at different scan rates. In both materials, the anodic and cathodic peak currents increase with increased scan rate, and the enhanced reversibility is demonstrated by their improved redox peak symmetry. Additionally, a small shift in the oxidation peak positions toward positive potential indicates that both electrode materials have less polarization.³⁸

The electrode dynamics in both materials are better examined using the power law relationship, by using equation 3,²⁷

$$i_p = av^b \quad (3)$$

Here i_p is the peak current, v is the scan rate, and a and b are arbitrary constants obtained from the fitting. Now, equation 3 can be modified as equation 4.

$$\log(i_p) = \log(a) + b\log(v) \quad (4)$$

In this case, the capacitive and diffusion-controlled contributions can be evaluated using the slope b , which can be computed from a linear fit of the plot between $\log(v)$ and $\log(i_p)$ (**Fig. 7c**). According to **Fig. 7c**, the b values of NWO and WNO materials are found to be 0.84 and 0.86, respectively, suggesting that, both capacitive and diffusive processes govern the sodium ion storage mechanism. Furthermore, equation 5 provides the quantitative distribution of the diffusive and capacitive contributions to the overall storage mechanism in both materials.²⁷

$$i(V) = k_1v + k_2v^{1/2} \quad (5)$$

Here, the surface capacitive and diffusion-controlled contributions are denoted by k_1v and $k_2v^{1/2}$, respectively. **Fig. 7d** and **e** display the capacitive and diffusive contributions on the CV plots of



the NWO and WNO electrodes, respectively, at a scan rate of $0.4 \text{ mV}\cdot\text{s}^{-1}$. **Fig. 7f** makes it evident that, in both materials the fraction of capacitive contribution gradually rises as the scan rate increases from 0.4 to $1 \text{ mV}\cdot\text{s}^{-1}$. This is because under higher rate conditions, surface capacitance dominates the total capacity. Concurrently, the diffusion-regulated capacity contribution decreases because the slow intercalation speed is unable to satisfy the needs of the high rate of electrochemical processes at higher scan rates.³⁹ Thus, the carbon-coated materials, NWO and WNO delivered enhanced electrochemical performance because of their improved structural defects, large specific surface area, pore size and high Na^+ -ion diffusion coefficient.

4. Conclusion

The present work proposes carbon-coated, TTB-type niobium tungstates, $\text{Nb}_{18}\text{W}_{16}\text{O}_{93}$ and $\text{Nb}_7\text{W}_{10}\text{O}_{47}$ as new sodium insertion materials. The anode materials were successfully synthesized via a facile hydrothermal-annealing process. As a result, the Nb-rich carbon-coated material, NWO demonstrated a high discharge capacity of $163.95 \text{ mA}\cdot\text{h}\cdot\text{g}^{-1}$ at $10 \text{ mA}\cdot\text{g}^{-1}$, whereas the W-rich material, WNO, achieved a significant capacity retention of more than 81%. Here, the Nb-dominant material offered different charge/discharge profiles and slightly a higher specific capacity may be due to more sites available for sodium, but the W-dominant material offered better structural stability and more consistent performance possibly due to being a more readily confirmed stable phase. The slow capacity fading observed in the material, NWO was explained with respect to its higher charge transfer resistance compared to WNO. Niobium tungsten oxides are thus highlighted in this paper as intriguing anode options for the advancement of high-performance SIB technology.



Author contributions

Y. Bhaskara Rao: Investigation, Methodology, Conceptualization, Formal analysis, Data curation, Writing- original draft. **Katta Vamsi Krishna:** Investigation, Visualization. **C. André Ohlin:** Validation, Supervision, Resources, Visualization, Funding acquisition, Writing- review & editing, Project administration.

Conflicts of interest

The authors declare no competing financial interest.

Data availability

Any data that support the findings of this study are included within the article.

Acknowledgement

Authors thank the Kempe foundation (JCSMK22-0094 and JCSMK24-511) and the Swedish Research Council (VR 2023-04608) for financial support and acknowledge the Multi-purpose Adaptive X-ray Scattering platform (MAXS) for instrument access and technical support and Umeå Centre for Electron Microscopy (UCEM) for the facilities and technical assistance at the Chemical Biological Centre (KBC), Umeå University, SWEDEN. The authors also thank Dr. Solomon Tesfalidet (UmU) for invaluable technical assistance.



References

- 1 Z. Xue, S. Yang, S. Zhang, L. Xing, S. Lee, H. S. Park, C. Yan and J. Huang, *Energy Mater. Adv.*, 2025, **6**, 0415.
- 2 J. Bai, Z. Li, X. Wang, S. Konrad, C. Wu and H. Zhao, *Energy Mater. Adv.*, 2024, **5**, 0086.
- 3 M. Chen, Q. Liu, S. Wang, E. Wang, X. Guo and S. Chou, *Adv. Energy Mater.*, 2019, **9**, 1803609.
- 4 D. Fan, Q. Shen, H. Li, X. Qu, L. Jiao and Y. Liu, *Energy Mater. Adv.*, 2024, **5**, 0073.
- 5 E. Irisarri, A. Ponrouch and M. R. Palacin, *J. Electrochem. Soc.*, 2015, **162**, A2476–A2482.
- 6 H. Kang, Y. Liu, K. Cao, Y. Zhao, L. Jiao, Y. Wang and H. Yuan, *J. Mater. Chem. A*, 2015, **3**, 17899–17913.
- 7 Q. Deng, Y. Fu, C. Zhu and Y. Yu, *Small*, 2019, **15**, 1804884.
- 8 S. Y. Lee, A. S. Lim, Y. M. Kwon, K. Y. Cho and S. Yoon, *Inorg. Chem. Front.*, 2020, **7**, 3176–3183.
- 9 H. Li and H. Zhou, *Chem. Commun.*, 2012, **48**, 1201–1217.
- 10 Y. B. Rao and C. A. Ohlin, *Sustain. Energy Fuels*, 2025, **9**, 2217–2227.
- 11 G. Chen, J. Chen, I. P. Parkin, G. He and T. S. Miller, *ChemElectroChem*, 2022, **9**, e202200800.
- 12 Y. Subramanian, G. K. Veerasubramani, M. S. Park and D. W. Kim, *Mater. Lett.*, 2022, **314**, 131891.
- 13 K. J. Griffith, K. M. Wiaderek, G. Cibin, L. E. Marbella and C. P. Grey, *Nature*, 2018, **559**, 556–563.



- 14 C. P. Kocer, K. J. Griffith, C. P. Grey and A. J. Morris, *Chem. Mater.*, 2020, **32**, 3980–3989.
- 15 F. Krumeich, *Crystals*, 2021, **11**, 1514.
- 16 F. Krumeich and M. Worle, *Z. Anorg. Allg. Chem.*, 2025, **651**, e202500033.
- 17 S. Nagendran, B. Wen, C. P. Grey, S. Nagendran, A. Mahadevegowda, S. Vema and M. Danaie, *Matter*, 2024, **7**, 3567–3586.
- 18 C. Cai, P. McCormack, Z. Nie and G. M. K. Jr, *J. Electrochem. Sci. Eng.*, 2023, **13**, 641–658.
- 19 R. Xia, C. Sun, Y. Wang, D. M. Cunha, H. Peng, K. Zhao, M. Huijben and J. E. ten Elshof, *J. Power Sources*, 2021, **482**, 228898.
- 20 F. Krumeich, M. Worle and A. Hussain, *J. Solid State Chem.*, 2000, **149**, 428–433.
- 21 C. Yue, X. Zhu, M. Rigutto and E. Hensen, *Appl. Catal. B Environ.*, 2015, **163**, 370–381.
- 22 Y. B. Rao and C. A. Ohlin, *RSC Adv.*, 2025, **15**, 34300–34309.
- 23 Y. Yang, H. Zhu, J. Xiao, H. Geng, Y. Zhang, J. Zhao, G. Li, X. L. Wang, C. C. Li and Q. Liu, *Adv. Mater.*, 2020, **32**, 1905295.
- 24 R. Hou, B. Liu, Y. Sun, L. Liu, J. Meng, M. D. Levi, H. Ji and X. Yan, *Nano Energy*, 2020, **72**, 104728.
- 25 Y. Da Cho, G. T. K. Fey and H. M. Kao, *J. Power Sources*, 2009, **189**, 256–262.
- 26 C. Corbella, E. Bertran, M. C. Polo, E. Pascual and J. L. Andujar, *Diam. Relat. Mater.*, 2007, **16**, 1828–1834.
- 27 Y. Bhaskara Rao, N. Tavajohi and C. Andre Ohlin, *Batter. Supercaps*, 2025, **8**, e202500134.
- 28 S. Shetty, R. Karmakar, S. D. Sutar, S. Narayanasamy, S. Aravind, A. Swami and S.



- Sinha, *ACS Appl. Nano Mater.*, 2025, **8**, 23308–23325.
- 29 Y. Xia, M. Yoshio and H. Noguchi, *Electrochim. Acta*, 2006, **52**, 240–245.
- 30 A. Safartoobi, J. Mazloom and F. E. Ghodsi, *J. Energy Storage*, 2023, **68**, 107818.
- 31 P. Chithaiah, R. C. Sahoo, J. H. Seok, S. U. Lee, H. S. S. R. Matte and C. N. R. Rao, *ACS Appl. Mater. Interfaces*, 2023, **15**, 45868–45875.
- 32 Y. Zhao, Z. Feng, Y. Tan, Q. Deng and L. Yao, *Nanomaterials*, 2024, **14**, 631.
- 33 Y. B. Rao, N. Tavajohi and C. A. Ohlin, *Mater. Adv.*, 2026, **7**, 1691–1703.
- 34 C. J. Y. X. Liu Ya-ting, Li Li-bing, Li Xin-xin, Miao Yong-xia, *Mod. Chem. Ind.*, 2025, **45**, 163–170.
- 35 S. Khatua, K. R. Achary, Y. B. Rao, K. Sasikumar, A. K. Samal and L. N. Patro, *New J. Chem.*, 2024, **48**, 18277–18290.
- 36 C. Liu, N. Xiao, Y. Wang, H. Li, G. Wang, Q. Dong, J. Bai, J. Xiao and J. Qiu, *Fuel Process. Technol.*, 2018, **180**, 173–179.
- 37 J. Ni, W. Wang, C. Wu, H. Liang, J. Maier, Y. Yu and L. Li, *Adv. Mater.*, 2017, **29**, 1605607.
- 38 B. He, J. Cunha, Z. Hou, G. Li and H. Yin, *J. Colloid Interface Sci.*, 2023, **650**, 857–864.
- 39 S. Li, J. Qiu, C. Lai, M. Ling, H. Zhao and S. Zhang, *Nano Energy*, 2015, **12**, 224–230.



Any data that support the findings of this study are included within the article.

Open Access Article. Published on 15 April 2026. Downloaded on 4/15/2026 8:39:07 PM.
This article is licensed under a Creative Commons Attribution 3.0 Unported Licence.

